



HAL
open science

Observational Quantification of Three-dimensional Anisotropies and Scalings of Space Plasma Turbulence at Kinetic Scales

Tieyan Wang, Jiansen He, Olga Alexandrova, Malcolm Dunlop, Denise Perrone

► **To cite this version:**

Tieyan Wang, Jiansen He, Olga Alexandrova, Malcolm Dunlop, Denise Perrone. Observational Quantification of Three-dimensional Anisotropies and Scalings of Space Plasma Turbulence at Kinetic Scales. *The Astrophysical Journal*, 2020, 898, 10.3847/1538-4357/ab99ca . insu-03717009

HAL Id: insu-03717009

<https://insu.hal.science/insu-03717009>

Submitted on 8 Jul 2022

HAL is a multi-disciplinary open access archive for the deposit and dissemination of scientific research documents, whether they are published or not. The documents may come from teaching and research institutions in France or abroad, or from public or private research centers.

L'archive ouverte pluridisciplinaire **HAL**, est destinée au dépôt et à la diffusion de documents scientifiques de niveau recherche, publiés ou non, émanant des établissements d'enseignement et de recherche français ou étrangers, des laboratoires publics ou privés.



Distributed under a Creative Commons Attribution 4.0 International License



Observational Quantification of Three-dimensional Anisotropies and Scalings of Space Plasma Turbulence at Kinetic Scales

Tieyan Wang¹ , Jiansen He² , Olga Alexandrova³, Malcolm Dunlop^{1,4}, and Denise Perrone⁵ ¹RAL Space, Rutherford Appleton Laboratory, Harwell Oxford, Didcot OX11 0QX, UK; tieyan.wang@gmail.com²School of Earth and Space Sciences, Peking University, Beijing 100871, People's Republic of China³LESIA, Observatoire de Paris, Université PSL, CNRS, Sorbonne Université, Univ. Paris Diderot, Sorbonne Paris Cité, 5 place Jules Janssen, F-92195 Meudon, France⁴School of Space and Environment, Beihang University, Beijing 100191, People's Republic of China⁵ASI—Italian Space Agency, via del Politecnico snc, I-00133 Rome, Italy

Received 2020 March 23; revised 2020 May 20; accepted 2020 June 3; published 2020 July 27

Abstract

A statistical survey of spectral anisotropy of space plasma turbulence is performed using five years of measurements from the Magnetospheric Multiscale mission in the magnetosheath. By measuring the five-point second-order structure functions of the magnetic field, we have for the first time quantified the three-dimensional anisotropies and scalings at sub-ion scales (<100 km). In the local reference frame $(\hat{L}_\perp, \hat{L}_\parallel)$ defined with respect to local mean magnetic field \mathbf{B}_0 , the “statistical eddies” are found to be mostly elongated along \mathbf{B}_0 and shortened in the direction perpendicular to both \mathbf{B}_0 and local field fluctuations. From several d_i (ion inertial length) toward $\sim 0.05 d_i$, the ratio between eddies' parallel and perpendicular lengths features a trend of rise then fall, whereas the anisotropy in the perpendicular plane appears scale-invariant. Specifically, the anisotropy relations for the total magnetic field at 0.1 – $1.0 d_i$ are obtained as $l_\parallel \simeq 2.44 \cdot l_\perp^{0.71}$, and $L_\perp \simeq 1.58 \cdot l_\perp^{1.08}$, respectively. Our results provide new observational evidence to compare with phenomenological models and numerical simulations, which may help to better understand the nature of kinetic-scale turbulence.

Unified Astronomy Thesaurus concepts: [Space plasmas \(1544\)](#); [Interplanetary turbulence \(830\)](#)

1. Introduction

The energy distribution at a certain scale (or \mathbf{k} space) is known to be not isotropic in the turbulence of magnetized plasma, also known as spectral anisotropy (Cho & Vishniac 2000). This particular feature reflects the preferential direction of the energy cascade with respect to the local background magnetic field \mathbf{B}_0 (Podesta 2009). Most of our experimental knowledge of space plasma anisotropy comes from in situ observations made within the solar wind (SW), which is a nearly collisionless plasmas stream released from the Sun (Bruno & Carbone 2013).

At large magnetohydrodynamic (MHD) scales, the pattern of correlation function for the magnetic field at 1 au has two major components referred to as the “Maltese cross,” exhibiting elongations in both parallel and perpendicular directions with regard to \mathbf{B}_0 (Matthaeus et al. 1990). This signature is summarized as the “slab+2D” model, which assumes no specific nature of the fluctuations but just describes the fluctuations as a combination of waves with k_\parallel and structures with k_\perp . Another type of anisotropy model is based on “critical-balance (CB)” conjecture, where the key hypothesis relies on the comparable scale of the linear Alfvén time and turbulence nonlinear time in a vanishing cross-helicity system (Goldreich & Sridhar 1995). As a result, the spectral anisotropy scales as $k_\parallel \propto k_\perp^{2/3}$. By introducing the idea of “dynamic alignment” between magnetic and velocity field fluctuations, Boldyrev (2006) modified the nonlinear time and established the 3D anisotropic turbulence model, where the eddies have

three different coherent scales. Indeed, numerous observations have found agreement between measurements and CB theories (Horbury et al. 2008; Luo & Wu 2010; Chen et al. 2011, 2012). Despite this consistency, recent studies of anisotropy in the solar wind reported some puzzling results and raised more concerns to be considered, such as intermittency (Wang et al. 2014; Pei et al. 2016; Yang et al. 2017), discrepancy between velocity field and magnetic field anisotropy (Wicks et al. 2011; Yan et al. 2016; Wu et al. 2019a, 2019b), dependence on the heliocentric distance (He et al. 2013), and solar wind expansion (Vech & Chen 2016; Verdini et al. 2018, 2019). Moreover, the 3D self-correlation functions are shown to be isotropic in Wang et al. (2019b) and Wu et al. (2019a, 2019b). Therefore, the anisotropic nature of the solar wind at MHD scales is still an open question.

At kinetic scales, the turbulence still remains or becomes much more anisotropic (i.e., Chen et al. 2010; Oughton et al. 2015 and references therein). The standard kinetic Alfvén wave (KAW) turbulence model, also on the basis of CB conjecture assuming the linear KAW propagation time to be comparable to nonlinear time, predicts an anisotropy scaling of $k_\parallel \propto k_\perp^{1/3}$ (Howes et al. 2008; Schekochihin et al. 2009). Moreover, it is important to pay attention to the plasma kinetic effects contributing to the spectral anisotropy at kinetic regime (see the review by Alexandrova et al. 2013 and Alexandrova et al. 2020). For example, the modified KAW turbulence model with intermittent 2D structures has $k_\parallel \propto k_\perp^{2/3}$ (Boldyrev & Perez 2012). Zhao et al. (2016) suggested a model for kinetic-scale Alfvénic turbulence that incorporates the dispersion and intermittency effects. In their model, the anisotropy scalings range from $1/3$ to $7/6$ at different scenarios. Boldyrev & Loureiro (2019) considered the decisive role played by the tearing instability in setting the aspect ratio of eddies and hence



Original content from this work may be used under the terms of the [Creative Commons Attribution 4.0 licence](#). Any further distribution of this work must maintain attribution to the author(s) and the title of the work, journal citation and DOI.

predicted the spectral anisotropy scalings between $k_{\parallel} \lesssim k_{\perp}^{2/3}$ and $k_{\parallel} \lesssim k_{\perp}$. Most recently, Landi et al. (2019) proposed a phenomenological model considering the intermittent two-dimensional structures in the plane perpendicular to \mathbf{B}_0 . In their model, the prescribed perpendicular aspect ratio of these structures could determine the anisotropy as $k_{\parallel} \propto k_{\perp}^{1/3(\alpha+1)}$, where α is proportional to the space-filling of the turbulence.

In recent high-resolution three-dimensional kinetic simulations, the spectral anisotropy has received considerable attention (Franci et al. 2018; Grošelj et al. 2018; Arzamasskiy et al. 2019; Cerri et al. 2019; Landi et al. 2019). Based on different methods of measuring the anisotropy, dissimilar scaling relations have been found (i.e., $k_{\parallel} \propto k_{\perp}^{1/3}$ in Grošelj et al. 2018 and $k_{\parallel} \propto k_{\perp}$ in Arzamasskiy et al. 2019). Specifically, for the analysis based on multipoint local structure functions (SF), which will be introduced in Section 2, the anisotropy tends to become “frozen” when approaching ion scales (i.e., $k_{\parallel} \propto k_{\perp}^{0.8}$ in Landi et al. 2019). By comparing the results from three different simulations including the hybrid particle-in-cell (PIC), Eulerian hybrid-Vlasov, and fully kinetic PIC codes, Cerri et al. (2019) found that the anisotropy scalings tend to converge to $l_{\parallel} \propto l_{\perp}^{2/3}$ based on a unified analysis of five-point SFs.

The Earth’s magnetosheath (MSH) offers a unique lab to study kinetic turbulence that is different from SW, such as its enhanced compressibility, intermittency, and kinetic instabilities (Alexandrova 2008; Zhu et al. 2019). In addition, the spacecraft measurements in MSH tend to cover a wider range of angle between bulk flow velocity and \mathbf{B}_0 as compared with solar wind (He et al. 2011), thus allowing us to diagnose the 3D nature of the fluctuations in a relatively short interval. Using Cluster measurements, Mangeney et al. (2006) surveyed four events and discovered the strong anisotropy of the electromagnetic fluctuations for the first time, with k_{\perp} extending for two decades within the kinetic range $kd_e \in [0.3, 30]$. Sahraoui et al. (2006) directly showed the anisotropic behavior up to $k\rho_i = 3.5$ in a mirror structure event by disentangling the spatial fluctuations from the temporal ones through four spacecraft. Alexandrova et al. (2008) further investigated the events of Mangeney et al. (2006) and found the dominance of 2D turbulence ($k_{\perp} \gg k_{\parallel}$) above the spectral break in the vicinity of the ion scale. Since these events cover different plasma conditions, the conclusion is believed to be universal. In addition, due to the sampling effects, the magnetic fluctuations have more energy along the $\mathbf{B} \times \mathbf{V}$ direction in their analysis. Similar 2D turbulence at kinetic scales was observed in a recent statistical study of magnetic field turbulence in the solar wind (Lacombe et al. 2017). He et al. (2011) computed the spatial correlation functions of both magnetic field and density fluctuations in the 2D (l_{\parallel}, l_{\perp}) plane, it is shown that the turbulence close to ion scales is comprised of two populations, where the major component is mostly transverse and the minor one is oblique. Using measurements from the Magnetospheric Multiscale mission (MMS; Burch et al. 2016), Chen & Boldyrev (2017) studied the two-point SF of the magnetic field in the same plane and provided evidence of strong anisotropy at scales $11 < k\rho_i < 57$. Another event recorded by MMS show that parameters such as magnetic field, density, ion velocity, and ion thermal speed all exhibit anisotropy in the spectral index at scales $k\rho_i \leq 1$ (Roberts et al. 2019).

Despite these case studies, a comprehensive in situ measurement of the kinetic-scale 3D anisotropy is still lacking.

Moreover, to our knowledge, the investigations concerning the scale-dependency of the anisotropy, especially the scaling relations, have not been made yet. The intention of this paper is to address these issues. Based on MMS measurement of magnetic field and ion velocity with unprecedented time resolution, we applied for the first time five-point second-order SF to statistically quantify the 3D anisotropy of the magnetic turbulence at the sub-proton scale (< 100 km). The new observational evidence we obtained, such as the empirical relations of the anisotropy scalings, can be compared with recent theoretical and numerical results, which may facilitate our understanding of kinetic-scale turbulence in the space plasmas.

The paper is organized as follows. We describe the data and methods in Section 2, present a typical event with three-dimensional anisotropy in Section 3, provide the statistical results in Section 4, and summarize and discuss our results in Section 5.

2. Data and Methods

The burst mode data from four MMS spacecraft, including magnetic field (128 Hz) from the FIELD instrument (Russell et al. 2016) and ion moments (6.7 Hz) from the FPI instrument (Pollock et al. 2016) are used in this study. 349 MSH intervals from 2015 September to 2019 December have been selected for the statistical analysis, whereas a 10 minute event on 4 October 2017 is presented to show a typical event with anisotropy signatures.

To quantify the anisotropy, we use the five-point second-order SF in this study. Compared with two-point SF, five-point SF is more suitable for studying spectral anisotropy at the sub-ion regime since it is less susceptible to leakage and influence from large scales (Cho 2019; Landi et al. 2019; W. H. Matthaeus 2020, private communication). More details of the difference between multipoint SFs are provided in Appendix A.

The five-point SF is the ensemble average of the squared variation Δf from five-point; as a function of displacement \mathbf{l} , the $S_2^{(5)}(\mathbf{l}; f)$ is defined as

$$S_2^{(5)}(\mathbf{l}; f) = \langle |\Delta f(\mathbf{r}, \mathbf{l})|^2 \rangle_{\mathbf{r}}. \quad (1)$$

The spatial variation from five-point is measured as

$$\Delta f(\mathbf{r}, \mathbf{l}) = [f(\mathbf{r} - 2\mathbf{l}) - 4f(\mathbf{r} - \mathbf{l}) + 6f(\mathbf{r}) - 4f(\mathbf{r} + \mathbf{l}) + f(\mathbf{r} + 2\mathbf{l})] / \sqrt{35}, \quad (2)$$

where Δf can represent perpendicular, parallel, or total magnetic field fluctuations, $\langle \dots \rangle_{\mathbf{r}}$ is the ensemble average over positions \mathbf{r} .

By studying the three-dimensional distribution of the $S_2^{(5)}(\mathbf{l}; f)$ with respect to \mathbf{l} , the “statistical shape” of the eddies in turbulence can be thus inferred from the contours of $S_2^{(5)}(\mathbf{l}; f)$.

In the computation, the velocity field is used to link the timescale with space displacement as $\mathbf{l} = \tau \cdot \mathbf{V}$ according to the Taylor hypothesis (Taylor 1938), which has been tested in Appendix B to be valid for most of our events. Here \mathbf{V} can be adopted as the mean velocity \mathbf{V}_{mean} during the interval of interest or considered as the local velocity field $\mathbf{V}_{\text{local}}$, where \mathbf{V} is interpolated on the resolution of \mathbf{B} in the calculation. Most previous works performed in solar wind and magnetosheath use \mathbf{V}_{mean} for simplicity (i.e., Chen et al. 2010, 2012; Chen & Boldyrev 2017; Wang et al. 2019b; Wu et al. 2019a). Also, the study of electron scale magnetic field structure functions is based on \mathbf{V}_{mean} (Chen & Boldyrev 2017). In a recent paper by

Verdini et al. (2018) the authors have considered the effects of local velocity by using $\mathbf{V}_{\text{local}}$ in their analysis of velocity field structure functions. We use five-point $\mathbf{V}_{\text{local}}$ in this paper, which is defined as $\mathbf{V}_{\text{local}} = [\mathbf{V}(\mathbf{r} - 2\mathbf{l}) + 4\mathbf{V}(\mathbf{r} - \mathbf{l}) + 6\mathbf{V}(\mathbf{r}) + 4\mathbf{V}(\mathbf{r} + \mathbf{l}) + \mathbf{V}(\mathbf{r} + 2\mathbf{l})]/16$. For the small spatial scales considered here, let us rewrite $\mathbf{l} = \tau \cdot \mathbf{V}$ as $\mathbf{l} = \tau \cdot (\mathbf{V}_0 + \delta\mathbf{V})$. Since τ is small, the major contribution of the velocity term is from the large-scale mean velocity \mathbf{V}_0 . In other words, the resolution of \mathbf{V} is not the key factor for interring \mathbf{l} , since it only determines $\delta\mathbf{V}$, whose amplitude is generally much smaller than \mathbf{V}_0 in the magnetosheath environment under this study. To verify this point, we have performed and compared the analyses on the basis of \mathbf{V}_{mean} and $\mathbf{V}_{\text{local}}$, and the results turn out to be nearly identical. Hence, we justify that the effects of interpolating \mathbf{V} at the time points of \mathbf{B} , or only considering \mathbf{V}_{mean} is negligible in the analysis of small-scale magnetic field structure functions.

Once the SF with respect to \mathbf{l} is computed, it can be projected into local coordinates with respect to the local magnetic field $\mathbf{B}_{\text{local}}$ as in Chen et al. (2012) and Verdini et al. (2018) to study its 3D features. These coordinates allow us to compare the results with recent simulations on the basis of the same reference frame (Ceri et al. 2019; Landi et al. 2019), and is consistent with the previous choice of studying spectral anisotropy at various scales (Chen et al. 2012; Chen & Boldyrev 2017; Verdini et al. 2018; Wu et al. 2019a). In the Cartesian coordinates system ($\hat{L}_\perp, \hat{l}_\perp, \hat{l}_\parallel$), \hat{l}_\parallel is along $\mathbf{B}_{\text{local}} = [\mathbf{B}(\mathbf{r} - 2\mathbf{l}) + 4\mathbf{B}(\mathbf{r} - \mathbf{l}) + 6\mathbf{B}(\mathbf{r}) + 4\mathbf{B}(\mathbf{r} + \mathbf{l}) + \mathbf{B}(\mathbf{r} + 2\mathbf{l})]/16$, \hat{L}_\perp is the "displacement direction" along $\delta\mathbf{B}_\perp = \mathbf{B}_{\text{local}} \times [\delta\mathbf{B} \times \mathbf{B}_{\text{local}}]$, and $\hat{l}_\perp = \hat{l}_\parallel \times \hat{L}_\perp$. The Cartesian system can also be converted into the spherical polar coordinates system as $(l, \theta_B, \phi_{\delta B_\perp})$, where θ_B represents the angle between $\mathbf{B}_{\text{local}}$ and \mathbf{l} , and $\phi_{\delta B_\perp}$ represents the angle between L_\perp and the projection of \mathbf{l} on the plane perpendicular to $\mathbf{B}_{\text{local}}$. Similar to Chen et al. (2012), angles greater than 90° are reflected below 90° to improve scaling measurement accuracy. Specifically, by setting the ranges of θ_B and $\phi_{\delta B_\perp}$, the SF in the three orthogonal directions can be obtained as

$$S_2^{(5)}(L_\perp; f) \equiv S_2^{(5)}(L_\perp; f, 85^\circ < \theta_B < 90^\circ, 0^\circ < \phi_{\delta B_\perp} < 5^\circ) \quad (3)$$

$$S_2^{(5)}(l_\perp; f) \equiv S_2^{(5)}(l_\perp; f, 85^\circ < \theta_B < 90^\circ, 85^\circ < \phi_{\delta B_\perp} < 90^\circ) \quad (4)$$

$$S_2^{(5)}(l_\parallel; f) \equiv S_2^{(5)}(l_\parallel; f, 0^\circ < \theta_B < 5^\circ, 0^\circ < \phi_{\delta B_\perp} < 90^\circ). \quad (5)$$

By equating the value between pairs of $S_2(l_\perp)$, $S_2(l_\parallel)$, and $S_2(L_\perp)$, we could infer the anisotropy relation between l_\perp , l_\parallel , and L_\perp .

3. Example of Local 3D Turbulence

Here we present an example with clear signatures of 3D anisotropy. The event is observed downstream of the quasi-parallel shock during 08:02:13–08:12:33 on 2017 October 4. Figure 1 shows the overview of the event. As plotted in Figures 1(a)–(b), the magnetic field is around 6.08 (0.61, 0.06, 0.79) \pm (4.1, 3.6, 3.8) nT, exhibiting numerous large directional changes while keeping its magnitude. In contrast, the ion velocity is quite stable at 288 (−0.88, 0.46, 0.07) \pm (15.5, 10.2, 13.5) km s^{−1}. Figure 1(c) shows the instantaneous increment of the total magnetic energy δB^2 as a function of scale and time. The magnitude of δB^2 generally increases with

the increase of scales and is changing intermittently with time. Similar to δB^2 , the instantaneous increments of the perpendicular energy δB_\perp^2 and parallel energy δB_\parallel^2 also exhibit the same trend with respect to spatial scale as seen in Figures 1(d)–(e), while the former one is stronger. Figures 1(f)–(g) plot the corresponding θ_B and $\phi_{\delta B_\perp}$, respectively. Due to the rapid rotations of magnetic field, the distribution of θ_B and $\phi_{\delta B_\perp}$ covers a wide range within (0, π) during the whole interval, thus allowing us to infer the 3D anisotropy of magnetic turbulence with sufficient data points.

Figure 2 presents the structure functions and the corresponding anisotropy scalings for the above event. The values of SFs are obtained from four MMS spacecraft, then binned and averaged. Each bin is required to have a minimum number of 200 data points to ensure reliable results as in Chen et al. (2010). For the SF of the total magnetic field energy as projected in the $(l_\parallel, \sqrt{l_\perp^2 + L_\perp^2})$ plane, the contours of $S_2^{(5)}(\mathbf{l}; \mathbf{B})$ are elongated in the parallel directions (Figure 2(a)), where the values in the perpendicular direction are much larger than the ones in the parallel direction (i.e., $S_2^{(5)}(\mathbf{l}; \mathbf{B})$ at $l_\perp = 60$ km is more than 100 times larger than the one at $l_\parallel = 60$ km). This signature indicates sub-ion-scale ($l < 2 d_i$) anisotropy with $k_\perp \gg k_\parallel$ and is in agreement with Mangeney et al. (2006), Alexandrova et al. (2008), and Chen & Boldyrev (2017). Furthermore, we find that the contours of $S_2^{(5)}(\mathbf{l}; \mathbf{B})$ are also elongated in the "displacement" direction as seen in the (l_\perp, L_\perp) plane (Figure 2(b)), suggesting the three-dimensional characteristics of the anisotropy. In addition to $S_2^{(5)}(\mathbf{l}; \mathbf{B})$, we also consider the contribution of SF by the perpendicular and parallel magnetic field, namely the $S_2^{(5)}(\mathbf{l}; \mathbf{B}_\perp)$ and $S_2^{(5)}(\mathbf{l}; \mathbf{B}_\parallel)$. As seen in Figures 2(c)–(d), the patterns for the contours of $S_2^{(5)}(\mathbf{l}; \mathbf{B}_\perp)$ are nearly comparable to those of $S_2^{(5)}(\mathbf{l}; \mathbf{B})$ in Figures 2(a)–(b). But the contours in Figure 2(e) are flatter than the ones in Figure 2(c), meaning the anisotropy of $S_2^{(5)}(\mathbf{l}; \mathbf{B}_\parallel)$ is slightly stronger than $S_2^{(5)}(\mathbf{l}; \mathbf{B}_\perp)$ in the $(l_\parallel, \sqrt{l_\perp^2 + L_\perp^2})$ plane. The much-elongated compressive fluctuations along \mathbf{B}_0 are consistent with solar wind observations in Chen et al. (2010, 2011, 2012), which may imply the less damped state of the more anisotropic fluctuations. On the contrary, the contours of $S_2^{(5)}(\mathbf{l}; \mathbf{B}_\parallel)$ are roughly isotropic in the (L_\perp, L_\parallel) plane, representing the 2D nature of the parallel fluctuations.

Let us draw the attention of the reader to the point that the sampling of SFs in the perpendicular and parallel directions is dissimilar as seen in Figure 1(f), whereas the parallel data are discretely distributed. To test whether the stationarity of the sampling will have an effect on the results of SFs, we have divided the time-series into two subintervals and analyze the SFs separately. During Interval 1 (08: 02: 13–08: 07: 13 UT), the measurements along parallel directions (i.e., $\theta_B < 5^\circ$) are less than the ones at oblique directions ($\theta_B > 50^\circ$). In contrast, during Interval 2 (08: 07: 13–08: 12: 33 UT), the measurements along parallel directions are frequent and the overall sampling is more homogeneous than Interval 1. As expected, the SFs for Interval 1 have no measurements within the range of $60 \text{ km} < l_\parallel < 100 \text{ km}$, $0 \text{ km} < \sqrt{l_\perp^2 + L_\perp^2} < 18 \text{ km}$, while the SFs for Interval 2 cover the complete wavenumber space. More importantly, the extension feature of the contours along the l_\parallel direction in these two subintervals appears quite similar as compared with the results from the whole interval. Hence, the anisotropic features of the turbulence could be viewed as stationary regardless of the interval selection. In fact, as the first

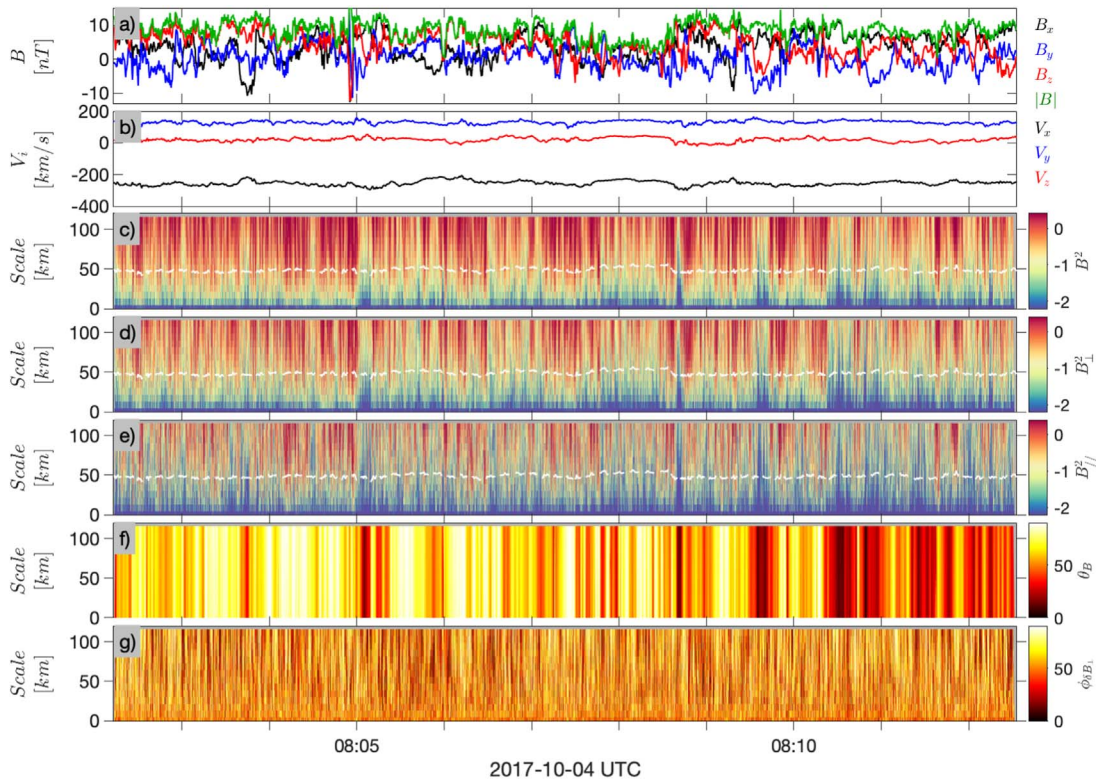


Figure 1. Event overview. (a) Three components and the strength of the magnetic field. (b) Three components of velocity field. (c)–(e) Instantaneous total, perpendicular, and parallel magnetic energy as a function of scale and time, overplotted with ion inertial length in white lines. (f) Instantaneous angle between local magnetic field and space displacement vector l , as a function of scale and time. (g) Instantaneous angle between L_{\perp} and the projection of l on the plane perpendicular to local magnetic field.

step of computing SFs , we calculate the time difference between continuous sampling points rather than discontinuous sampling points. As the second step, the calculated time differences satisfying certain θ_B conditions are collected together from discretely (discontinuously) distributed time points. This discontinuous collection will not significantly influence the analysis results as long as the whole time interval is statistically time stationary.

To inspect the scale-dependency of the anisotropy more precisely, we have computed the SF in the three orthogonal directions as defined by Equations (3)–(5). For the 1D SF of the total magnetic field shown in Figure 2(g), the relation of $S_2(l_{\perp}) > S_2(L_{\perp}) > S_2(l_{\parallel})$ is satisfied at all scales as expected, thus confirming the 3D nature of anisotropy again. Moreover, this anisotropy is found to be scale-dependent. For example, at an energy level of 0.01 nT^2 , the perpendicular length of the “statistical eddy,” $l_{\perp} \sim 6 \text{ km}$ is smaller than the “displacement” length $L_{\perp} \sim 8 \text{ km}$, while the parallel length is much larger at $l_{\parallel} \sim 35 \text{ km}$. The energy level increase to 1 nT^2 , l_{\perp} , L_{\perp} , and l_{\parallel} becomes approximately 60 km , 90 km , and 150 km , respectively. The change of the $l_{\perp} : L_{\perp} : l_{\parallel}$ ratio from $0.17 : 0.23 : 1$ to $0.4 : 0.6 : 1$ suggests that as scales increase, the anisotropy between parallel and perpendicular lengths becomes weak, while the anisotropy between two perpendicular lengths in the perpendicular plane remains almost unchanged. Setting an energy range to $[0.01, 0.5] \text{ nT}^2$, the SFs could be fitted by the power laws as $l_{\perp}^{1.92}$, $L_{\perp}^{1.82}$, and $l_{\parallel}^{3.08}$, where the standard error of the mean is 0.09 , 0.08 , 0.10 , respectively. The power-law index of the second-order structure function, g , is usually related to the power spectral index, α , by $\alpha = g + 1$ (Chen et al. 2010). Hence the spectral indices in the three directions are 2.92 , 2.82 ,

and 4.08 , respectively. The perpendicular spectral indices are close to 2.8 and steeper than $7/3$, which are consistent with previous findings both in the MSH and SW (Alexandrova et al. 2008, 2009; Huang et al. 2014; Chen & Boldyrev 2017; Matteini et al. 2017). For the SFs of δB_{\perp} , the trends plotted in Figure 2(i) are essentially the same compared with the results of δB in Figure 2(g), suggesting a dominant contribution of perpendicular magnetic field fluctuations to SFs. This point agrees with the “variance anisotropy” found in Chen et al. (2010) and is again supported by examining SFs of δB_{\parallel} in Figure 2(k), whose magnitudes are weaker than SFs of δB_{\perp} in Figure 2(g).

Figure 2(h) displays the anisotropy relations for δB , where the blue curve represents l_{\parallel} versus l_{\perp} and the red curve represents L_{\perp} versus l_{\perp} . On one hand, as the perpendicular scales decrease from $1.0 d_i$ to under $0.05 d_i$, the ratio of l_{\parallel}/l_{\perp} first increases and reaches a maximum of ~ 8 at $\sim 0.1 d_i$, whereas the anisotropy scaling obeys $l_{\parallel} \propto l_{\perp}^{0.67}$. Then the ratio of l_{\parallel}/l_{\perp} begins to decrease and finally approaches 1 at $\sim 0.04 d_i$. On the other hand, the ratio of L_{\perp}/l_{\perp} keeps steady around 1.5 , obeying $L_{\perp} \propto l_{\perp}^{1.09}$. As expected, the anisotropy relations for δB_{\perp} as shown in Figure 2(j) is quite similar to the relations in Figure 2(h), following $l_{\parallel} \propto l_{\perp}^{0.59}$ and $L_{\perp} \propto l_{\perp}^{1.05}$. Nevertheless, the anisotropy relations for δB_{\parallel} as shown in Figure 2(l) are dissimilar, following $l_{\parallel} \propto l_{\perp}^{0.93}$ and $L_{\perp} \propto l_{\perp}^{1.01}$.

4. Statistical Analysis of the Anisotropy Scalings

In this section, the sub-ion-scale anisotropy relations are investigated comprehensively based on a statistical survey of 349 intervals during 2015–2019, when MMS instruments were

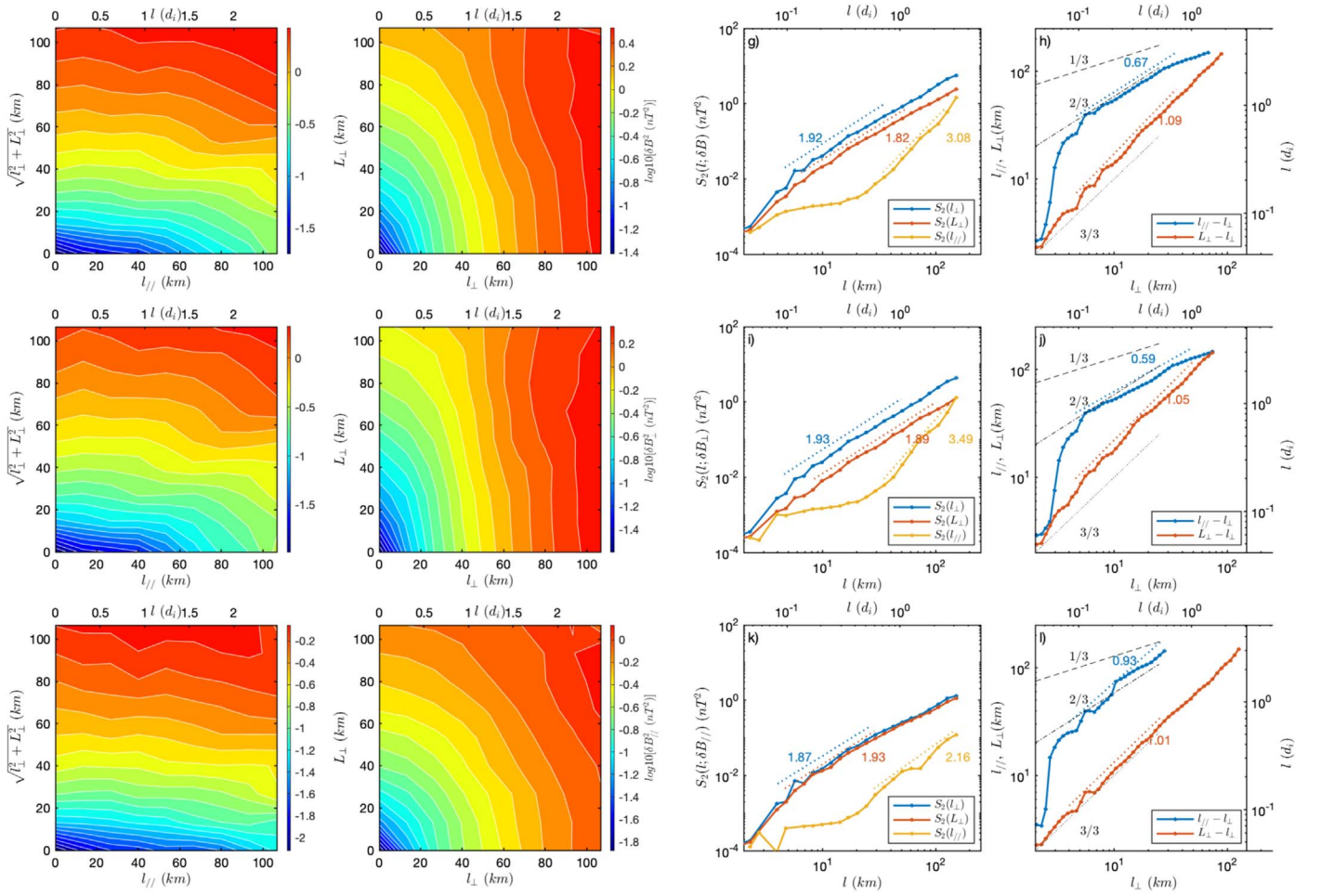


Figure 2. SFs in the 2D plane, together with the 1D SFs and their anisotropy scalings. The left two columns include (1) 2D SFs as a function of $(l_{\parallel}, \sqrt{l_{\perp}^2 + L_{\perp}^2})$ and (2) SFs as a function of $(L_{\perp}, L_{\parallel})$. The right two columns plot, respectively, (1) 1D SF as a function of l_{\perp} , L_{\perp} , and l_{\parallel} , and the relations between l_{\parallel} , L_{\perp} , and L_{\parallel} . For each panel, the first, second, and third rows represent SFs of the total, perpendicular, and parallel magnetic fields, respectively.

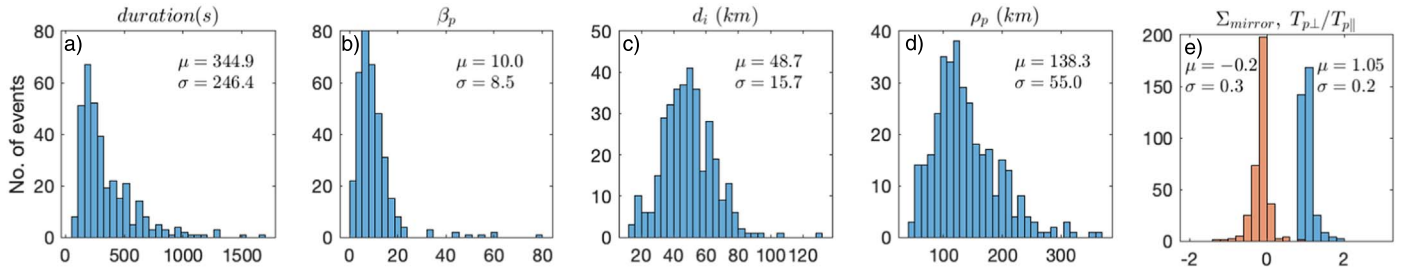


Figure 3. Histograms of the event duration and plasma characteristic parameters.

in burst mode. These intervals are tagged as “magnetosheath” on the MMS science data center website. In addition, to avoid the influence of shock or magnetopause, the ion and electron energy spectrograms have been checked by eye to make sure they exhibit typical broadband MSH signatures and are time stationary. As a result, 349 intervals with an average duration of ~ 5.8 minutes have been selected. Figure 3 shows the histograms for the event duration and plasma parameters, together with their mean value and standard deviations. The event duration, proton beta β_p , ion inertial length d_i , and proton gyroradius ρ_p , cover the range of [60, 1680] s, [0.3, 80], [15, 130] km, and [45, 370] km respectively. The mean value of temperature anisotropy $T_{p\perp}/T_{p\parallel}$ is 1.05. The distribution of mirror mode threshold $\Sigma_{mirror} = T_{p\perp}/T_{p\parallel} - 1/\beta_{p\perp} - 1$ is also

shown in Figure 3(e). Since most of the values are negative, the influence of mirror instability is not strong in our database.

Figure 4 presents the statistical results of the anisotropy relations. Concerning the parallel–perpendicular anisotropy of the total magnetic field δB , as revealed by the unique feature of the superimposed results in Figure 4(a), a large proportion of events exhibit an analogous trend. For the median value of the data, when the scales decrease from 10 d_i to 0.01 d_i , the anisotropy level as reflected from the vertical deviation from the isotropy reference line, displays a trend of rise then fall, with the break point occurring near 0.1 d_i . The fit of an empirical anisotropy relation $l_{\parallel} = a_0 \cdot l_{\perp}^{\alpha}$ yield a_0 of 2.44 and a scaling of $\alpha_l = 0.71 \pm 0.03$ at large scales within [0.1, 1] d_i . Compared with three reference scaling-laws of $\alpha = 1/3, 2/3,$ and $3/3$, the fitted scaling is closer

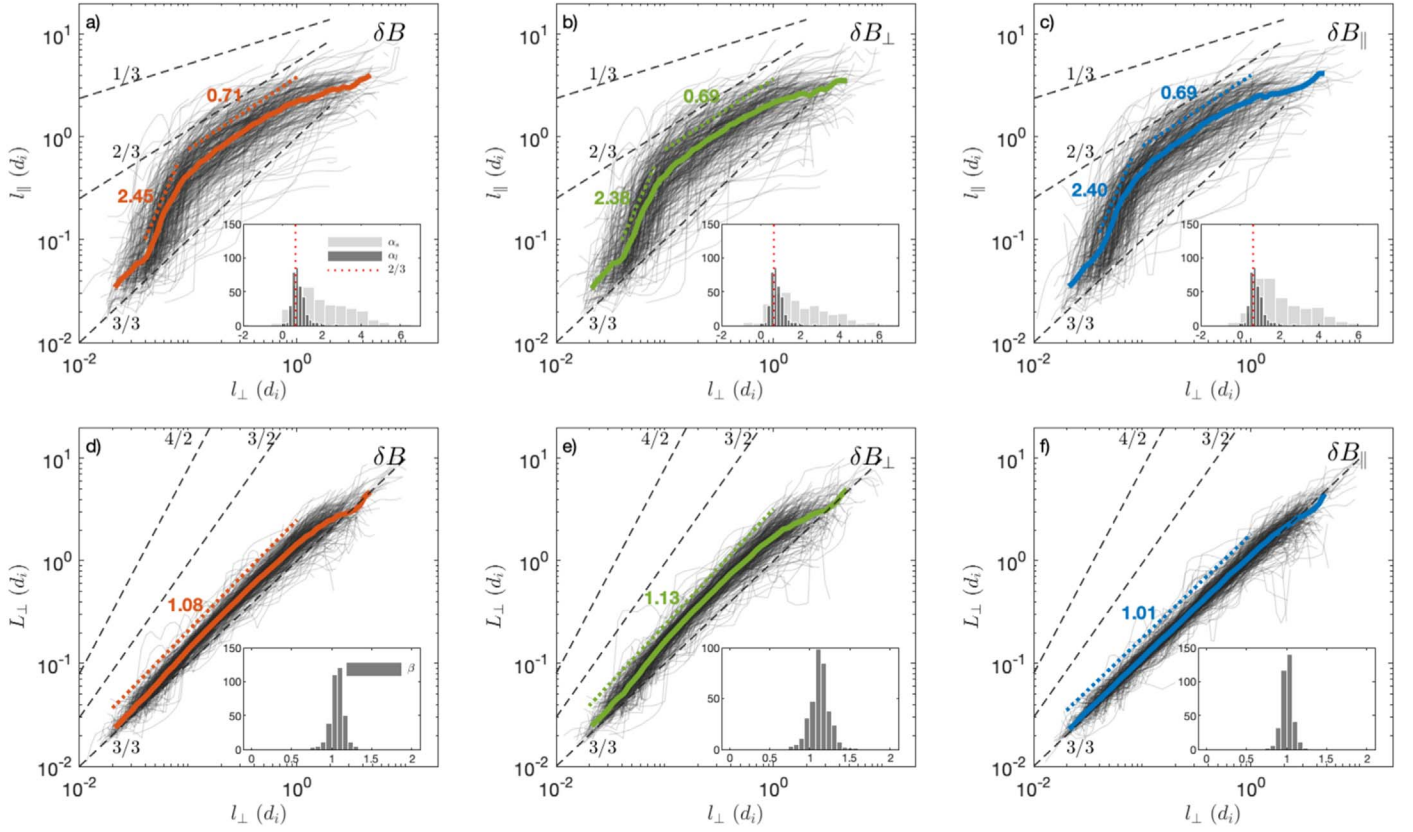


Figure 4. Statistical analysis of the 3D anisotropy scalings. The first, second, and third columns show, respectively, the anisotropy of δB , δB_{\perp} , and δB_{\parallel} . The light gray curves represent the superposition of the statistical results, the median value, and fitted results are overlotted in bold solid and dotted lines. The dashed lines represent specifically the reference scalings with slopes of 1/3, 2/3, 1 in the top panels, and 4/2, 3/2, 1 in the bottom panels. The histogram of the anisotropy scalings at $0.04 d_i$ – $0.08 d_i$ (light gray), and $0.1 d_i$ – $1.0 d_i$ (dark gray) are inserted in top panels. Similarly, the histograms of the anisotropy at $0.02 d_i$ – $1.0 d_i$ (light gray) are inserted in the bottom panels.

to $2/3$. At smaller scales within $[0.04, 0.08] d_i$, we find $a_0 = 170$, and $\alpha_s = 2.45 \pm 0.35$. Likewise, the anisotropy relations of δB_{\perp} and δB_{\parallel} in Figures 4(b)–(c) display similar trends as Figure 4(a), where the anisotropy scalings at $[0.1, 1.0] d_i$ are obtained as $\alpha_l = 0.69 \pm 0.03$ and $\alpha_l = 0.69 \pm 0.04$ and the scalings at $[0.04, 0.08] d_i$ are $\alpha_s = 2.38 \pm 0.32$ and $\alpha_s = 2.40 \pm 0.14$, respectively. By examining the distribution of power-law scalings for each individual event as shown in the histograms in Figure 4, we confirm that for the scalings at $[0.1, 1.0] d_i$ (dark gray), a summary of over 100 events have a scaling centered near $2/3$ (red dotted lines). However, as shown in the light gray histogram of the scalings at $[0.04, 0.08] d_i$, the scalings are broadly distributed within $[0, 4]$.

Regarding the anisotropy of δB and δB_{\perp} in the perpendicular plane, Figures 4(d)–(e) show that for most of the data, although $L_{\perp} > L_{\parallel}$, the anisotropy level is stable since the scalings are close to 1. In addition, the empirical relation $L_{\perp} = b_0 \cdot l_{\perp}^{\beta}$ for the median value are fitted as $L_{\perp} = 1.58 \cdot l_{\perp}^{1.08 \pm 0.01}$, $L_{\perp} = 2.03 \cdot l_{\perp}^{1.13 \pm 0.02}$ at $[0.02, 1.0] d_i$, respectively. Lastly, the anisotropy for δB_{\parallel} vanishes and follows a nearly isotropic relation of $L_{\perp} = 1.15 \cdot l_{\perp}^{1.01 \pm 0.003}$.

5. Conclusion and Discussion

In this paper, we have conducted a statistical survey of the sub-ion-scale anisotropy of the turbulence in the Earth’s magnetosheath. By measuring the five-point second-order SFs of the magnetic field, the three-dimensional structures of the turbulence

have been quantitatively characterized. Specifically, the three characteristic lengths of the eddies are found to roughly satisfy $l_{\parallel} > L_{\perp} > L_{\parallel}$ in the local reference frame defined by Chen et al. (2012). As for the scale-dependency of the anisotropy inferred from SFs of the total magnetic field, (1) the parallel–perpendicular anisotropy as revealed by the ratio of l_{\parallel}/l_{\perp} , shows an increasing trend toward small scales and obeys a scaling of $l_{\parallel} \simeq 2.44 \cdot l_{\perp}^{0.71}$ between $0.1 d_i$ and $1 d_i$, then it decreases and obeys $l_{\parallel} \simeq 170 \cdot l_{\perp}^{2.45}$ between $0.04 d_i$ and $0.08 d_i$; and (2) the anisotropy in the perpendicular plane, as revealed by the ratio of L_{\perp}/l_{\perp} , is generally weaker than the ratio of l_{\parallel}/l_{\perp} . Moreover, this anisotropy is scale-invariant, displaying a scaling of $L_{\perp} \simeq 1.58 \cdot l_{\perp}^{1.08}$.

Interestingly, the parallel–perpendicular anisotropy tends to become increasingly isotropic when approaching both large scales $\sim 4 d_i$ and small scales $\sim 0.04 d_i$ (Figures 4(a)–(c)). This large-scale isotropy may reflect similar structures as in the isotropic solar wind reported recently (i.e., Wang et al. 2019b; Wu et al. 2019a, 2019b), while the small-scale isotropy has not been reported before to our knowledge. Possible explanations for isotropy include the weakening of perpendicular cascade and the influence of ion cyclotron waves. Indeed, there are a few events with $l_{\perp} > l_{\parallel}$ in the database, where the existence of ICW has been confirmed by checking the polarization state of the fluctuations. In a few other events, we also find coexistence of ICW and 2D $l_{\parallel} > l_{\perp}$ structures through inspecting the SFs in the 2D $(l_{\parallel}, l_{\perp})$ plane.

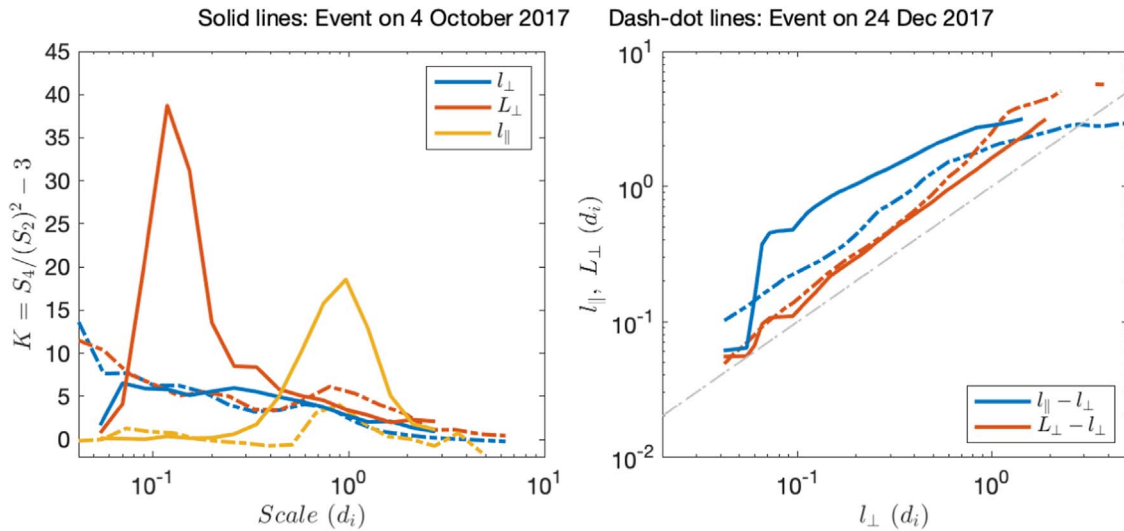


Figure 5. Comparisons of the intermittency and anisotropy relation between two events during 08: 02: 13–08: 12: 33 on 2017 October 4 and 01: 04: 43–01: 11: 53 on 2017 December 24.

The scaling of $l_{\parallel} \propto l_{\perp}^{0.71}$ observed in this work is different from traditional KAW theory of $l_{\parallel} \propto l_{\perp}^{1/3}$, but is close to the theoretical prediction of $l_{\parallel} \propto l_{\perp}^{2/3}$ from Boldyrev & Perez (2012) and Boldyrev & Loureiro (2019) and the simulation from Cerri et al. (2019). It also corresponds to $\alpha = 1.13$ in the framework of the model by Landi et al. (2019). Hence a modified CB premise may be needed to understand the kinetic turbulence in magnetosheath. We note that, for most of the events, the weak and scale-independent anisotropy in the perpendicular plane appears to agree with recent PIC simulation of KAW turbulence (D. Grošelj 2020, private communication) but is inconsistent with results of Boldyrev & Loureiro (2019), which predicts a much stronger anisotropy and a steeper scaling of $L_{\perp} \propto l_{\perp}^{3/2}$ or $L_{\perp} \propto l_{\perp}^2$, depending on different current sheet configurations for the tearing instability. Capturing the active signatures of current sheet disruption/reconnection (i.e., Mallet et al. 2017, Loureiro & Boldyrev 2017) from in situ observation is a challenging task, but will contribute to understanding its effects on the anisotropy.

The spectral anisotropy of kinetic plasma turbulence is believed to be associated with dispersion and intermittency effects (Zhao et al. 2016; Landi et al. 2019). For example, the anisotropic scalings are different below and above ion cyclotron frequency and also differs for sheet and tube-like turbulence (Zhao et al. 2016). To illustrate the possible connection between intermittency and spectral anisotropy, we specifically compare the results from two events. Figure 5 shows the excess Kurtosis and anisotropy relation for the total magnetic field. The excess Kurtosis is defined as $K(l) = S_4(l)/S_2(l)^2 - 3$, where $S_4(l)$ is the fourth-order structure function. In both panels of Figure 5, the solid lines represent the results from event 1, which is recorded on 2017 October 4 and is used as our example of spectral anisotropy in Section 3, while the dashed–dotted lines represent the results from event 2, which is recorded on 2017 December 24. As plotted in three directions l_{\perp} , L_{\perp} , l_{\parallel} , the value of $K(l)$ is around zero at large scales, meaning the roughly Gaussian distribution of the fluctuations. Toward small scales, $K(l)$ displays an increase tendency before it drops down. Such non-Gaussian statistics ($K(l) > 0$) confirms the presence of intermittency in the magnetosheath, while the scale-dependent profile of

Kurtosis is similar with solar wind observations (He et al. 2019). For the kinetic-scale parallel–perpendicular anisotropy, we find that it can be considerably affected by the intermittency. As shown in Figure 5, the stronger the intermittency (see the larger Kurtosis of the solid lines in the left panel), the stronger the anisotropy level (see the larger vertical distances between the solid blue curve and the gray line in the right panel). This phenomenon is consistent with previously observations at large scales, which emphasize the key role of intermittency in generating the spectral anisotropy (i.e., Wang et al. 2014; Pei et al. 2016; Yang et al. 2018). For the anisotropy in the perpendicular plane, the anisotropy levels (see the two red curves in the right panel) of these two events are much smaller as compared with the parallel–perpendicular anisotropies. The reason for such weak anisotropy still remains to be explored. We note that it has been proposed that the axisymmetric, 2D ($k_{\perp} > k_{\parallel}$) fluctuations can be observed with nonaxisymmetric features in the spacecraft frame due to a sampling effect (i.e., Saur & Bieber 1999; Alexandrova et al. 2008; Turner et al. 2011; Lacombe et al. 2017 and Matteini et al. 2020). Therefore, the spectral anisotropy (nonaxisymmetric) in the perpendicular plane needs to be cautiously interpreted with such effects being quantitatively explored in the future. Lastly, we note that both of the events still have non-Gaussian fluctuations (as seen in the nonzero values of the Kurtosis), hence the absence of the isotropic $l_{\parallel} \approx L_{\perp} \approx l_{\perp}$ relation is not contradictory to previous studies, which found isotropy when the intermittency is removed (i.e., Pei et al. 2016). We plan to conduct a much more comprehensive analysis to understand how intermittency influences spectral anisotropy in a future work, particularly focusing on comparing the role of different coherent structures on the anisotropy (i.e., tube-like vortices in Jovanovic et al. 2020, Wang et al. 2019a, and Alexandrova et al. 2020 or current sheets in Stawarz et al. 2019).

The authors wish to thank William H. Matthaeus, Riddhi Bandyopadhyay, and Daniel Grošelj for useful discussions. We greatly appreciate the MMS development and operations teams, as well as the instrument PIs, for data access and support. T.-Y. W. was supported by the Marie Skłodowska-Curie grant No.

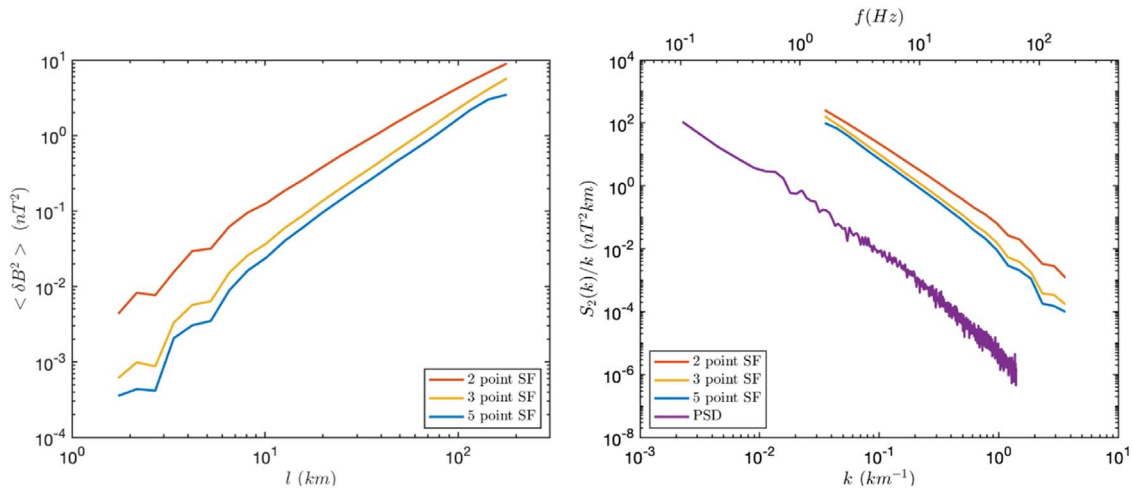


Figure 6. Comparison of multipoint structure functions during 08:02:13–08:12:33 on 2017 October 4.

665593 from the European Union’s Horizon 2020 research and innovation program. This work was also supported by the NSFC grants 41821003 and 41874193 and STFC in-house research grant ST/M001083/1. J.-S.H. is supported by NSFC under 41874200 and 41421003.

Appendix A

Comparison of Multipoint Structure Functions

The differences between multipoint second-order structure functions of the total magnetic field are compared here, where the two-point and three-point structure functions are defined as $S_2^{(2)}(l; f) = \langle |f(\mathbf{r} + l) - f(\mathbf{r})|^2 \rangle_r$, and $S_2^{(3)}(l; f) = 1/3 \langle |f(\mathbf{r} - l) - 2f(\mathbf{r}) + f(\mathbf{r} + l)|^2 \rangle_r$, respectively. As seen in the left panel of Figure 6, the trend of three-point and five-point SF tend to agree with each other, whereas the slope of two-point SF are relatively flatter, especially toward small scales. We also compute the “equivalent spectrum” defined as $S_2(k)/k$ and compare the results with power spectral density (PSD) from Fourier transform. Again, it is found that within $[0.05, 1] \text{ km}^{-1}$ of the right panel, the slope of the spectrum based on five-point SF is around -2.86 , which is similar to the three-point result of -2.80 and the slope of PSD around -2.94 , while the slope based on two-point SF is only -2.55 . Hence it is suggested that in order to capture the spectral characteristics of the turbulence at the sub-ion regime, the use of multipoint (>2) structure functions are preferred. Specifically, two-point SF could only diagnose the spectrum with a scaling up to 2, while five-point SF is capable of resolving a scaling up to 8 (Monin & Yaglom 1975; Cho & Lazarian 2009; Chen et al. 2010). In addition, the truncation error for the approximation with five-point central differentiation is known to be much smaller than the one based on two-point differentiation when reaching sufficient small scales.

We also note that, although the form of computing five-point SF resembles a finite-difference fourth derivative of the field, at sub-ion scales, the influence from “pre-whitening” of the signal might be weaker as compared to the analysis based on self-correlation functions (Bieber et al. 1993). Hence the

“post-darken” filter is not needed to diagnose the steep power law here. However, at the smallest scale (the Nyquist wavenumber), the validity of five-point SF still remains unknown (W. H. Matthaeus 2020, private communication) and we will verify it in the future.

Appendix B

Validity of the Taylor Hypothesis

At kinetic scales, the Taylor hypothesis may be violated by the significant fluctuations in the turbulent flows, or due to the large phase speed of the fluctuations exceeding the bulk flow velocity (e.g., Huang & Sahraoui 2019; Treumann et al. 2019). The validity of the Taylor hypothesis for all the events is checked by comparing the structure function of magnetic fluctuations in two ways (Chen & Boldyrev 2017): one is to calculate the structure function from single-spacecraft measurements by assuming Taylor hypothesis, and the other is to calculate the structure function based on direct spatial differences between measurements from six pairs of MMS spacecraft, which are separated by certain inter-distances between them.

Figure 7 shows the statistical results of the first-order structure function as a function of scale. As represented by a different color for each individual event, the results based on the Taylor hypothesis (curves) are close to the results from direct spatial measurements (crosses) at $5 \text{ km} < l < 200 \text{ km}$. Therefore, the use of the Taylor hypothesis in our analysis has been proven to be reasonable. We note that our results at small scales are in agreement with recent demonstration of the Taylor hypothesis being valid down to $kd_e \sim 1$ (Chen & Boldyrev 2017). In addition, the Taylor condition is known to be better satisfied at relatively large perpendicular wavenumbers especially when fluctuations are sampled along the perpendicular direction (Chen & Boldyrev 2017 and references therein), thus the presence of spectral anisotropy ($k_\perp > k_\parallel$) in our events is also in favor of the Taylor assumptions.

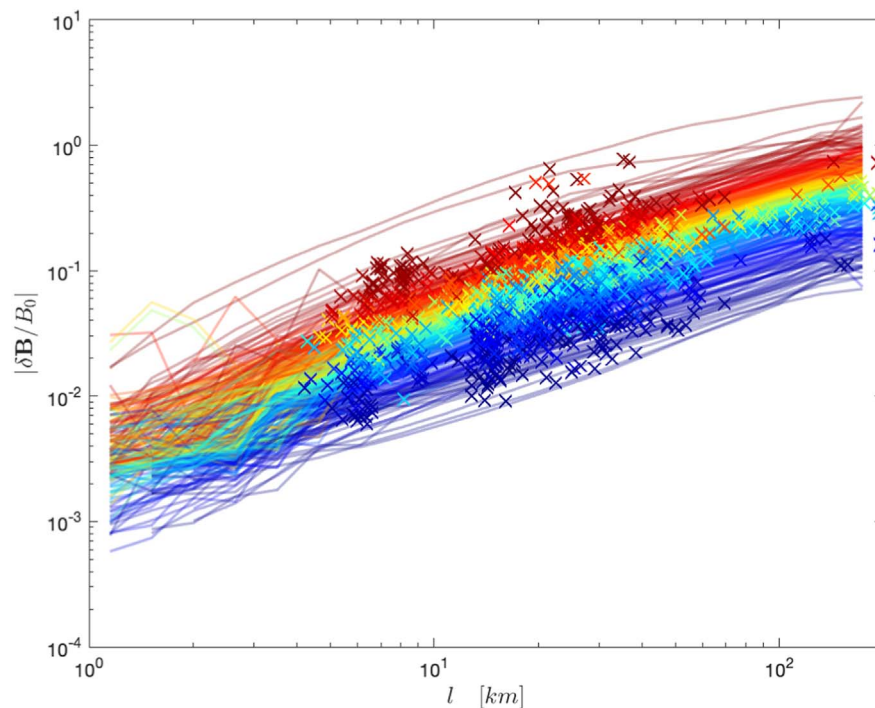


Figure 7. Test of validity of the Taylor hypothesis. The vertical axis represents the normalized magnetic fluctuation amplitudes obtained from first-order structure function. The curves are from the time differences of measurements from individual spacecraft under Taylor assumption, while the crosses are based on the spatial differences between measurements from the six pairs of MMS spacecraft.

ORCID iDs

Tieyan Wang  <https://orcid.org/0000-0003-3072-6139>
 Jansen He  <https://orcid.org/0000-0001-8179-417X>
 Denise Perrone  <https://orcid.org/0000-0003-1059-4853>

References

- Alexandrova, O. 2008, *NPGeo*, **15**, 95
 Alexandrova, O., Chen, C. H. K., Sorriso-Valvo, L., Horbury, T. S., & Bale, S. D. 2013, *SSRv*, **178**, 101
 Alexandrova, O., Krishna Jagarlamudi, V., Rossi, C., et al. 2020, arXiv:2004.01102
 Alexandrova, O., Lacombe, C., & Mangeney, A. 2008, *AnGeo*, **26**, 3585
 Alexandrova, O., Saur, J., Lacombe, C., et al. 2009, *PhRvL*, **103**, 165003
 Arzamasskiy, L., Kunz, M. W., Chandran, B. D. G., & Quataert, E. 2019, *ApJ*, **879**, 53
 Bieber, J. W., Chen, J., Matthaeus, W. H., Smith, C. W., & Pomerantz, M. A. 1993, *JGR*, **98**, 3585
 Boldyrev, S. 2006, *PhRvL*, **96**, 115002
 Boldyrev, S., & Loureiro, N. F. 2019, *PhRvR*, **1**, 012006
 Boldyrev, S., & Perez, J. C. 2012, *ApJL*, **758**, L44
 Bruno, R., & Carbone, V. 2013, *LRSP*, **10**, 2
 Burch, J. L., Moore, T. E., Torbert, R. B., & Giles, B. L. 2016, *SSRv*, **199**, 5
 Cerri, S. S., Grošelj, D., & Franci, L. 2019, *FrASS*, **6**, 64
 Chen, C. H. K., & Boldyrev, S. 2017, *ApJ*, **842**, 122
 Chen, C. H. K., Horbury, T. S., Schekochihin, A. A., et al. 2010, *PhRvL*, **104**, 255002
 Chen, C. H. K., Mallet, A., Schekochihin, A. A., et al. 2012, *ApJ*, **758**, 120
 Chen, C. H. K., Mallet, A., Yousef, T. A., Schekochihin, A. A., & Horbury, T. S. 2011, *MNRAS*, **415**, 3219
 Cho, J. 2019, *ApJ*, **874**, 75
 Cho, J., & Lazarian, A. 2009, *ApJ*, **701**, 236
 Cho, J., & Vishniac, E. T. 2000, *ApJ*, **539**, 273
 Franci, L., Landi, S., Verdini, A., Matteini, L., & Hellinger, P. 2018, *ApJ*, **853**, 26
 Goldreich, P., & Sridhar, S. 1995, *ApJ*, **438**, 763
 Grošelj, D., Mallet, A., Loureiro, N. F., & Jenko, F. 2018, *PhRvL*, **120**, 105101
 He, J., Tu, C., Marsch, E., Bourouaine, S., & Pei, Z. 2013, *ApJ*, **773**, 72
 He, J., Wang, Y., & Sorriso-Valvo, L. 2019, *ApJ*, **873**, 80
 He, J. S., Marsch, E., Tu, C. Y., et al. 2011, *JGRA*, **116**, A06207
 Horbury, T. S., Forman, M., & Oughton, S. 2008, *PhRvL*, **101**, 175005
 Howes, G. G., Cowley, S. C., Dorland, W., et al. 2008, *JGRA*, **113**, A05103
 Huang, S. Y., & Sahraoui, F. 2019, *ApJ*, **876**, 138
 Huang, S. Y., Sahraoui, F., Deng, X. H., et al. 2014, *ApJL*, **789**, L28
 Jovanovic, D., Alexandrova, O., Maksimovic, M., & Belic, M. 2020, *ApJ*, **896**, 8
 Lacombe, C., Alexandrova, O., & Matteini, L. 2017, *ApJ*, **848**, 45
 Landi, S., Franci, L., Papini, E., et al. 2019, arXiv:1904.03903
 Loureiro, N. F., & Boldyrev, S. 2017, *PhRvL*, **118**, 245101
 Luo, Q. Y., & Wu, D. J. 2010, *ApJL*, **714**, L138
 Mallet, A., Schekochihin, A. A., & Chandran, B. D. G. 2017, *MNRAS*, **468**, 4862
 Mangeney, A., Lacombe, C., Maksimovic, M., et al. 2006, *AnGeo*, **24**, 3507
 Matteini, L., Alexandrova, O., Chen, C. H. K., & Lacombe, C. 2017, *MNRAS*, **466**, 945
 Matteini, L., Franci, L., Alexandrova, O., et al. 2020, FrP, submitted
 Matthaeus, W. H., Goldstein, M. L., & Roberts, D. A. 1990, *JGR*, **95**, 20673
 Monin, A. S., & Yaglom, A. M. 1975, *Statistical Fluid Mechanics 2* (Cambridge, MA: MIT Press)
 Oughton, S., Matthaeus, W. H., Wan, M., & Osman, K. T. 2015, *RSPTA*, **373**, 20140152
 Pei, Z., He, J., Wang, X., et al. 2016, *JGRA*, **121**, 911
 Podesta, J. J. 2009, *ApJ*, **698**, 986
 Pollock, C., Moore, T., Jacques, A., et al. 2016, *SSRv*, **199**, 331
 Roberts, O. W., Narita, Y., Nakamura, R., Vörös, Z., & Gershman, D. 2019, *FrP*, **7**, 184
 Russell, C. T., Anderson, B. J., Baumjohann, W., et al. 2016, *SSRv*, **199**, 189
 Sahraoui, F., Belmont, G., Rezeau, L., et al. 2006, *PhRvL*, **96**, 075002
 Saur, J., & Bieber, J. W. 1999, *JGR*, **104**, 9975
 Schekochihin, A. A., Cowley, S. C., Dorland, W., et al. 2009, *ApJS*, **182**, 310
 Stawarz, J. E., Eastwood, J. P., Phan, T. D., et al. 2019, *ApJL*, **877**, L37
 Taylor, G. I. 1938, *RSPSA*, **164**, 476
 Treumann, R. A., Baumjohann, W., & Narita, Y. 2019, *EP&S*, **71**, 41

- Turner, A. J., Gogoberidze, G., Chapman, S. C., Hnat, B., & Müller, W. C. 2011, [PhRvL](#), **107**, 095002
- Vech, D., & Chen, C. H. K. 2016, [ApJL](#), **832**, L16
- Verdini, A., Grappin, R., Alexandrova, O., et al. 2019, [MNRAS](#), **486**, 3006
- Verdini, A., Grappin, R., Alexandrova, O., & Lion, S. 2018, [ApJ](#), **853**, 85
- Wang, T., Alexandrova, O., Perrone, D., et al. 2019a, [ApJL](#), **871**, L22
- Wang, X., Tu, C., & He, J. 2019b, [ApJ](#), **871**, 93
- Wang, X., Tu, C., He, J., Marsch, E., & Wang, L. 2014, [ApJL](#), **783**, L9
- Wicks, R. T., Horbury, T. S., Chen, C. H. K., & Schekochihin, A. A. 2011, [PhRvL](#), **106**, 045001
- Wu, H., Tu, C., Wang, X., He, J., & Wang, L. 2019a, [ApJ](#), **882**, 21
- Wu, H., Tu, C., Wang, X., He, J., & Wang, L. 2019b, [ApJL](#), **883**, L9
- Yan, L., He, J., Zhang, L., et al. 2016, [ApJL](#), **816**, L24
- Yang, L., He, J., Tu, C., et al. 2017, [ApJ](#), **846**, 49
- Yang, L., Zhang, L., He, J., et al. 2018, [ApJ](#), **855**, 69
- Zhao, J. S., Voitenko, Y. M., Wu, D. J., & Yu, M. Y. 2016, [JGRA](#), **121**, 5
- Zhu, X., He, J., Verscharen, D., & Zhao, J. 2019, [ApJ](#), **878**, 48